COMMUNICATION

Magnetic Resonance in Medicine 000:000–000 (2011)

Integration of Diffusion-Weighted MRI Data and a Simple Mathematical Model to Predict Breast Tumor Cellularity During Neoadjuvant Chemotherapy

Nkiruka C. Atuegwu,[1,2] Lori R. Arlinghaus,[1,2] Xia Li,[1,2] E. BrianWelch,[1,2] Bapsi A. Chakravarthy,[3,4] John C. Gore,[1–3,5–7] and Thomas E. Yankeelov[1–3,5,6,8*]

Diffusion-weighted magnetic resonance imaging data obtained early in the course of therapy can be used to estimate tumor proliferation rates, and the estimated rates can be used to predict tumor cellularity at the conclusion of therapy. Six patients underwent diffusion-weighted magnetic resonance imaging immediately before, after one cycle, and after all cycles of neoadjuvant chemotherapy. Apparent diffusion coefficient values were calculated for each voxel and for a whole tumor region of interest. Proliferation rates were estimated using the apparent diffusion coefficient data from the first two time points and then used with the logistic model of tumor growth to predict cellularity after therapy. The predicted number of tumor cells was then correlated to the corresponding experimental data. Pearson's correlation coefficient for the region of interest analysis yielded 0.95 ($P = 0.004$), and, after applying a 3 × 3 mean filter to the apparent diffusion coefficient data, the voxel-by-voxel analysis yielded a Pearson correlation coefficient of 0.70 ± 0.10 ($P < 0.05$). Magn Reson Med 000:000–000, 2011. ©2011 Wiley Periodicals, Inc.

Key words: diffusion MRI; cellularity; tumor growth; mathematical model; breast cancer

Neoadjuvant chemotherapy improves the likelihood of successful breast conservation surgery in patients with locally advanced breast cancer by potentially reducing tumor size at the time of surgery (1). Predicting the outcome of neoadjuvant chemotherapy early during the course of therapy may provide clinicians the ability to adjust treatment on an individual patient basis. One way to achieve this may be through the use of mathematical models. Mathematical models of tumor growth often require knowledge of parameters that may be difficult to measure noninvasively and spatially for individual patients, but in principle this limitation may be overcome through the use of noninvasive imaging. Here, we focus on using measurements made with diffusion-weighted magnetic resonance imaging (DW-MRI) to provide initial conditions for the logistic model of tumor growth.

The microscopic thermally induced behavior of molecules moving in a random pattern is referred to as self-diffusion or Brownian motion. The rate of diffusion in cellular tissues is described by the apparent diffusion coefficient (ADC), which largely depends on the number and separation of barriers that a diffusing water molecule encounters. MRI methods have been developed to map the ADC, and in well-controlled situations, the ADC has been shown to correlate inversely with tissue cellularity (2–6). Several clinical studies have confirmed the ability of ADC to report on changes in tumor cellularity in the breast after neoadjuvant chemotherapy (7–9). Investigators have used DW-MRI and its extension, diffusion tensor imaging, to model how brain tumors grow or respond to treatment. For example, Ellingson et al. used ADC values obtained at three time points for patients with glioblastoma to estimate parameters of the diffusion growth model, including the proliferation rate and the rate of diffusion of tumor cells (10). Other groups (11–14) have used diffusion tensor imaging to calculate some of the parameters of the diffusion growth model or extensions thereof for patients with brain tumors. However, these studies have not made explicit use of the biophysical relationships between ADC and cellular variations. Here, we build on previous work (15,16) to show how serial DW-MRI data can be used to calculate the proliferation rate of tumors for patients with localized invasive breast cancer. The calculated proliferation rates were used to simulate the tumor cell density at the time of a later DW-MRI exam allowing a direct comparison of the estimated and simulated tumor density at the latter time point.

MATERIALS AND METHODS

Data were acquired from six patients with locally advanced breast cancer who were enrolled in an ongoing clinical trial (9). The patients provided informed consent,

[1]Institute of Imaging Science, Vanderbilt University, Nashville, Tennessee, USA.

[2]Department of Radiology and Radiological Sciences, Vanderbilt University, Nashville, Tennessee, USA.

[3]Vanderbilt Ingram Cancer Center, Vanderbilt University, Nashville, Tennessee, USA.

[4]Department of Radiation Oncology, Vanderbilt University, Nashville, Tennessee, USA.

[5]Department of Physics and Astronomy, Vanderbilt University, Nashville, Tennessee, USA.

[6]Department of Biomedical Engineering, Vanderbilt University, Nashville, Tennessee, USA.

[7]Department of Molecular Physiology and Biophysics, Vanderbilt University, Nashville, Tennessee, USA.

[8]Department of Cancer Biology, Vanderbilt University, Nashville, Tennessee, USA.

Grant sponsor: National Institutes of Health; Grant numbers: NCI 1R01CA129961, NCI U01 CA142565, NCI P50 CA128323, NCI P30 CA68485

*Correspondence to: Thomas E. Yankeelov, Ph.D., Vanderbilt University Medical Center, Institute of Imaging Science, Vanderbilt University, AA-1105 Medical Center North, 1161 21st Avenue South, Nashville, TN 37232-2310. E-mail: thomas.yankeelov@vanderbilt.edu

Received 11 April 2011; revised 14 July 2011; accepted 11 August 2011.

DOI 10.1002/mrm.23203
Published online in Wiley Online Library (wileyonlinelibrary.com).

and the study was approved by our Institutional Review Board. The patients were enrolled on a study that involved neoadjuvant chemotherapy which consisted of 12 weekly cycles of cisplatin, paclitaxel, with or without RAD001. Dynamic contrast enhanced MRI (DCE-MRI) and DW-MRI of the patients were obtained before (t_1), after one cycle (t_2), and at the completion of neoadjuvant chemotherapy (t_3).

Imaging Protocol

DW-MRI and DCE-MRI were performed using a Philips 3T Achieva MR scanner (Philips Healthcare, Best, The Netherlands) equipped with a four-channel receive double-breast coil (Invivo Inc., Gainesville, FL).

DW-MRIs were acquired with a single-shot spin echo echo planar imaging sequence in three orthogonal diffusion encoding directions (x, y, and z), with two b values (50 and 600 s/mm^2 [500 s/mm^2 for one subject]), in-plane field of view = 192 mm × 192 mm (unilateral), an acquisition matrix of 96 × 96 reconstructed to 144 × 144, and 10 signal acquisitions. Sensitivity encoding (SENSE) parallel imaging (acceleration factor = 2) and spectrally selective adiabatic inversion recovery fat saturation were implemented to reduce image artifacts. Subjects were breathing freely with no gating applied. The patient DW-MRIs consisted of 12 sagittal slices with slice thickness = 5 mm (no slice gap), pulse repetition time = 3080 ms, echo time = 43 ms, diffusion time (Δ) = 20.7 ms, and diffusion gradient duration (δ) = 11.6 ms for a total scan time of 4 min and 40 s.

DCE-MRI data were acquired with a three-dimensional radiofrequency-spoiled gradient echo sequence with pulse repetition time/echo time = 7.9 ms/1.3 ms. The acquisition matrix was 192 × 192 × 20 over a sagittal field of view (25.6 cm)^2 with slice thickness of 5 mm, one signal acquisition, and a SENSE factor of 2. This scan was repeated for 10 flip angles (ranging from 2° to 20° in 2° increments) thereby generating data to estimate the precontrast T_1. The same protocol (with the flip angle fixed at 10°) was used for the dynamic study in which each 20-slice set was collected in 16 s at 25 time points. A catheter placed within an antecubital vein delivered 0.1 mmol/kg of Gadolinium diethylenetriamine pentaacetic acid (Gd-DTPA) (Magnevist, Berlex, Wayne, NJ) at a rate of 2 mL/s (followed by a saline flush) after the acquisition of the first three (baseline) dynamic scans.

Image Analysis

ADC maps were calculated from the DW-MRI data using Eq. 1:

$$\mathrm{ADC} = \frac{\sum_{i=x,y,z} \ln(S_0/S_i)/b_i}{3}, \qquad [1]$$

where i is the diffusion-weighting direction, b_i represents the amount of diffusion-weighting imparted to the sample, S_i is the measured signal in each voxel, and S_0 is the signal at the minimum b value (17). This analysis was performed for each patient and for each time point. To perform the modeling described below, it is imperative that the ADC maps be spatially coregistered across time points. The DCE-MRI data, which was also collected at the three time points, provided this capability. These data were non-rigidly registered to each other using an adaptive basis algorithm with a tumor volume preserving constraint (18,19). The DCE-MR and DW-MR images were collected at the same time with minimal patient motion so the images were inherently registered to each other. Thus, by registering the DCE data and applying the corresponding transformation to the DW-MRI data, the DW-MRI data are registered as well.

Once registered, the tumor region of interest (ROI) was manually drawn on the difference image between the averaged postcontrast and the averaged precontrast baseline images. The ROIs were drawn on multiple slices to cover the entire visible lesion. The enhanced voxels in the manually drawn ROI was used as the tumor voxels. A voxel was considered "enhanced" if its signal in the postcontrast image was greater than the signal in the baseline image by at least 40%. (The 40% cut-off was selected empirically; values of 30 or 50% did not significantly affect the results below.) The tumor ROI from the pretreatment scan (time point t_1) was then copied onto the images obtained at subsequent time points (t_2 and t_3).

Mathematical Modeling

For early times, the logistic model allows exponential growth of the tumor cells, whereas for later times, the tumor asymptotically approaches the limiting cellular carrying capacity for a given region of space (here, an imaging voxel). The logistic model is explained in detail in Ref. 20, and the relevant equation is

$$N(r,t) = \frac{\theta N(r,0)}{N(r,0) + (\theta - N(r,0))\mathrm{e}^{-k(r)t}}, \qquad [2]$$

where $N(r,t)$ is the number of cells per voxel at position r and time t, $N(r,0)$ is the number of cells present at $t = 0$ (first time point) and position r, $k(r)$ is the cell proliferative rate at position r, and θ is the cell carrying capacity of the population. Note that $k(r)$ can be negative or positive to describe cell death or proliferation, respectively, and therefore implicitly includes the effects of the treatment. To estimate the number of cells in each voxel at each time point, we used the ADC values of the voxels obtained from Eq. 1. Several studies have shown a strong negative correlation between ADC and cellularity (2–6). We therefore used this relationship to convert ADC values to tumor cell number. To do this conversion, we assumed that the voxels with an ADC value of free water will have no tumor cells and the voxel with the minimum ADC value will contain the maximum number of cells, θ. This allows us to define the following mapping between ADC and cell number as shown in Eq. 3:

$$\mathrm{ADC}(r,t) = \mathrm{ADC}_\mathrm{w} - \lambda N(r,t), \qquad [3]$$

where ADC_w is the ADC of free water and λ is a proportionality constant. To obtain λ, we assume that the minimum ADC, $\mathrm{ADC}_\mathrm{min}$, within the tumor occurs at the voxel that has reached the carrying capacity θ. The minimum ADC in the tumor ROI from t_1 and t_2 was used as the $\mathrm{ADC}_\mathrm{min}$. The carrying capacity is assumed to be the

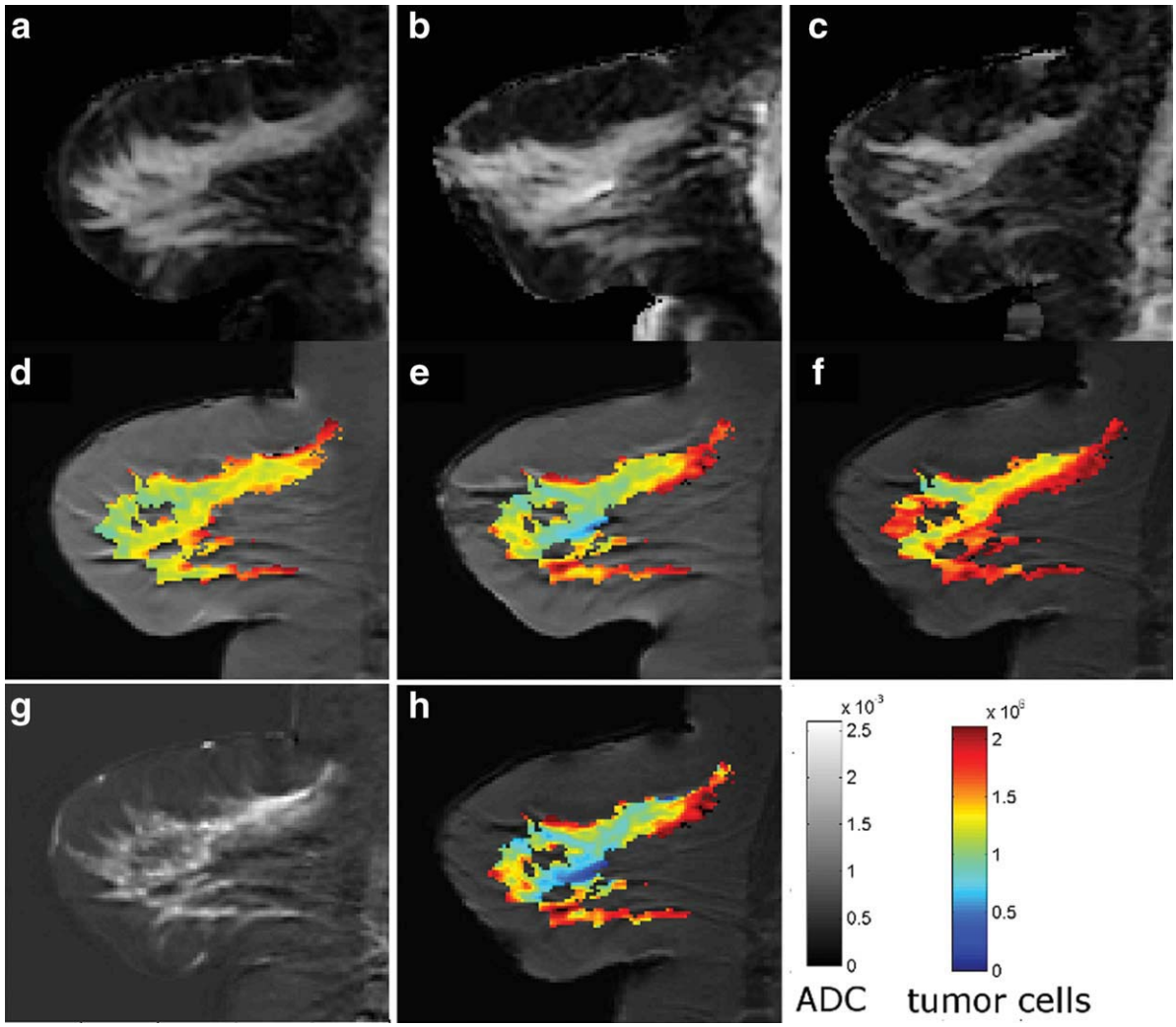

FIG. 1. Panels **a**, **b**, and **c** show the ADC maps (mm^2/s) of a cross section of the tumor for a representative patient before therapy (t_1), after one cycle of therapy (t_2), and at the conclusion of therapy (t_3), respectively. Panels **d**, **e**, and **f** show the estimated number of tumor cells at t_1, t_2, and t_3, respectively. Panel **g** is the difference image between the averaged postcontrast and the averaged precontrast baseline images from which the tumor ROI was drawn, and panel **h** is the simulated number of tumor cells as t_3.

maximum number of cells that can be contained in a voxel. This was calculated by dividing the voxel volume by the average cell volume of a (spherical) breast tumor cell. We assumed a nominal radius of 10 μm leading to a tumor cell volume of 4189 μm^3.

Combining the above assumptions with Eq. 3 results in Eq. 4:

$$\mathrm{ADC}_{\min} = \mathrm{ADC}_{\mathrm{w}} - \lambda\theta. \quad [4]$$

Combining Eqs. 2–4 gives Eq. 5 as previously described (16):

$$\left(\frac{\mathrm{ADC}(r,t) - \mathrm{ADC}_{\min}}{\mathrm{ADC}(r,t) - \mathrm{ADC}_{\mathrm{w}}}\right) = \left(\frac{\mathrm{ADC}(r,0) - \mathrm{ADC}_{\min}}{\mathrm{ADC}(r,0) - \mathrm{ADC}_{\mathrm{w}}}\right) e^{-k(r)t}. \quad [5]$$

The ADC data from t_1 and t_2 were used with Eq. 5 to calculate the proliferation rate $k(r)$ of the tumor cells in each voxel. The ADC values from t_2 and t_3 were then converted to tumor cell number $N_{\mathrm{estimated}}(r,t_2)$ and $N_{\mathrm{estimated}}(r,t_3)$, respectively, using Eqs. 3 and 4. The number of cells within the tumor at t_3 was then calculated via Eq. 2 using the calculated proliferation rate and $N_{\mathrm{estimated}}(r,t_2)$ to yield $N_{\mathrm{simulated}}(r,t_3)$. As the treatment was given weekly, the logistic model was run in a pulsed fashion whereby the model was switched "on" for the day of treatment, and switched "off" for all other times. At each iteration of the model (i.e., after each weekly cycle), a new number of cells for the end of the cycle were calculated. More specifically, for the first model update, $N_{\mathrm{estimated}}(r,t_2)$ and $k(r)$ were used in conjunction with Eq. 2 to calculate the number of cells at the end of the second cycle. The newly calculated number of cells was then used in conjunction with $k(r)$ to calculate the number of cells at the end of the third cycle. We allowed the tumor cells to proliferate according to the calculated proliferation rate only during the day of treatment; a point we return to in the "Discussion" section. This was repeated until the number of cells at the end of all cycles of treatment $N_{\mathrm{simulated}}(r,t_3)$ was calculated. The estimated and simulated values were then compared as described in the "Statistical Analysis" section.

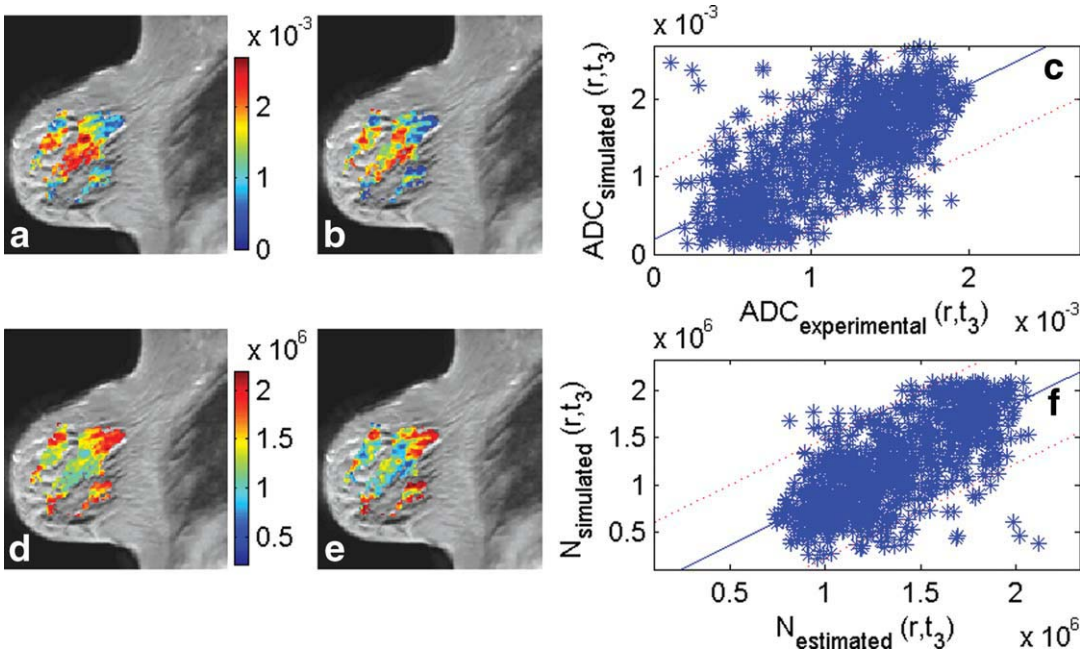

FIG. 2. Panels **a** and **b** show an overlay of the experimental and the simulated ADC (mm^2/s) values at day t_3, respectively, on a sagittal, T_1-weighted image. Panel **c** compares the experimental and the simulated ADC values at t_3 with the 95% confidence interval indicated by the dotted lines. Panels **d** and **e** are the estimated number of cells at t_3, $N_{estimated}(r,t_3)$ and the simulated number of cells at t_3, $N_{simulated}(r,t_3)$, respectively. Panel **f** compares the simulated and the estimated number of cells at t_3 with the 95% confidence interval indicated by the dotted lines. Pearson's and concordance correlation coefficients for the voxels in the slice are 0.71 and 0.63, respectively. The Pearson and concordance correlation coefficients for all the voxels within the tumor for this patient are 0.70 and 0.65, respectively.

In addition to the voxel-by-voxel comparisons between the estimated and simulated values, we also compared ROIs. To do this, the mean ADC values for each tumor ROI for each patient and for each time point were calculated. The mean ADC values for t_1 and t_2 were then used to calculate the mean proliferation rate, k_{mean}, using Eq. 5. The mean number of cells on t_2 and t_3, $N_{estimated\_mean}(t_2)$ and $N_{estimated\_mean}(t_3)$, respectively, were then calculated using Eqs. 3 and 4. $N_{estimated\_mean}(t_2)$ in conjunction with k_{mean} via Eq. 2 was used to calculate the simulated mean number of cells at t_3, $N_{simulated\_mean}(t_3)$. This was then compared to $N_{estimated\_mean}(t_3)$ as described below in the "Statistical Analysis" section.

Effects of Smoothing on Voxel Level Analysis

To explore the effects of the signal-to-noise ratio (SNR) and potential registration errors on the results of the modeling, we convolved the voxel level ADC values with a mean filter of varying kernel sizes. Convolving the ADC values with a mean filter removes spurious ADC values that are not representative of their surroundings. We used three different kernel sizes: [3 × 3], [6 × 6], and [9 × 9] with the degree of smoothing increasing with increasing kernel size. The ADC values obtained after smoothing were used to calculate new $k(r)$, $N_{estimated}(r,t_3)$, and $N_{simulated}(r,t_3)$ values for all patient data sets as described in the "Mathematical Modeling" section.

Statistical Analysis

Four different statistical analyses were performed on the data sets: the (1) Pearson correlation coefficient was used to compare voxel-based $N_{simulated}(r,t_3)$ and $N_{estimated}(r,t_3)$ values for each patient; (2) concordance correlation coefficient (21) was used to compare voxel-based $N_{simulated}(r,t_3)$ and $N_{estimated}(r,t_3)$ values for each patient; (3) Pearson correlation coefficient was calculated for the ROI-based $N_{simulated\_mean}(t_3)$ and $N_{estimated\_mean}(t_3)$ values for all the patients grouped together; (4) concordance correlation coefficient was calculated for the ROI-based $N_{simulated\_mean}(t_3)$ and $N_{estimated\_mean}(t_3)$ values for all the patients grouped together. Tests 1 and 2 were then repeated for the smoothed data.

RESULTS

Figure 1 shows the ADC maps, the estimated and simulated number of tumor cells, and the difference image between the averaged postcontrast and averaged precontrast image from which the tumor ROI was drawn for one of the patients. The minimum ADC value (ADC_{min}) used to calculate the carrying capacity of the tumor was slightly different for each patient. The values ranged from 0.1×10^{-3} to 0.5×10^{-3} mm^2/s with a mean value of 0.2×10^{-3} mm^2/s. Figure 2 shows the experimental and simulated ADC maps and the estimated and simulated number of cells at t_3 superimposed on the corresponding T_1-weighted MR image for a representative patient. Panels a and b show the experimental and the simulated ADC values at t_3, respectively. Panel c is a scatter plot of the data in panels a and b with the 95% confidence interval. Panels d and e are the estimated and simulated number of cells at t_3, $N_{estimated}(r,t_3)$, and $N_{simulated}(r,t_3)$, respectively, and panel f is a scatter plot

Table 1
Summary Statistics for the Six Patients

Patient	Mean $k \times 10^{-3}$ (1/day)	Mean ADC $(t_1) \times 10^{-3}$ (mm^2/s) ± SD	Mean $N_{estimated}$ $(t_3) \times 10^6$	Mean $N_{simulated}$ $(t_3) \times 10^6$	No filtering		3 × 3		6 × 6		9 × 9	
					PCC	CCC	PCC	CCC	PCC	CCC	PCC	CCC
P1	−0.96	1.62 ± 0.36	1.59	1.37	0.64	0.63	0.77	0.77	0.86	0.85	0.90	0.90
P2	0	1.44 ± 0.32	1.20	1.21	0.38	0.32	0.55	0.47	0.69	0.59	0.76	0.65
P3	−0.95	1.21 ± 0.33	1.76	1.55	0.44	0.32	0.61	0.46	0.72	0.55	0.78	0.60
P4	−19.9	0.99 ± 0.24	1.50	1.41	0.50	0.44	0.62	0.58	0.73	0.72	0.82	0.80
P5	−1.86	1.04 ± 0.33	1.64	1.51	0.70	0.65	0.81	0.76	0.89	0.84	0.92	0.87
P6	−30.3	1.39 ± 0.23	1.06	0.88	0.57	0.57	0.85	0.85	0.96	0.95	0.98	0.98
Mean ± 1.96SE	−9 ± 10.3	1.28 ± 0.20	1.46 ± 0.22	1.32 ± 0.20	0.54 ± 0.10	0.49 ± 0.12	0.70 ± 0.10	0.65 ± 0.13	0.81 ± 0.09	0.75 ± 0.13	0.86 ± 0.07	0.80 ± 0.12

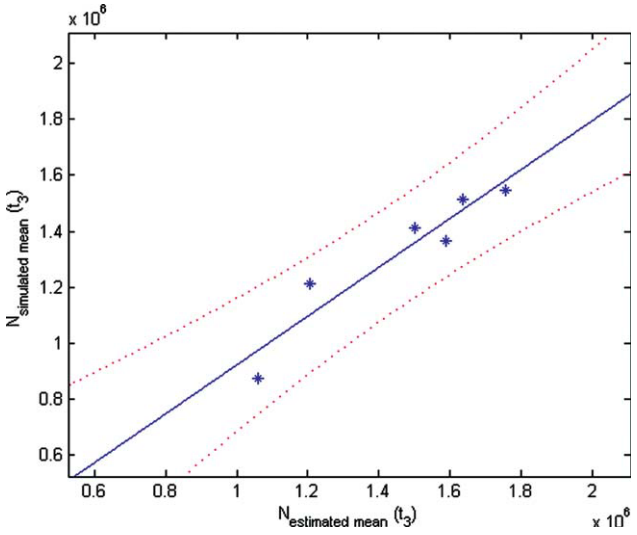

FIG. 3. The ROI average $N_{estimated\_mean}(t_3)$ versus $N_{simulated\_mean}(t_3)$ is plotted for all six patients with the 95% confidence interval displayed as dotted curves. Each point in the figure represents a single patient. Pearson's correlation coefficient between $N_{simulated\_mean}(t_3)$ and $N_{estimated\_mean}(t_3)$ for all the patients is 0.95 ($P = 0.004$), and the concordance correlation coefficient for all the patients is 0.83.

of $N_{estimated}(r,t_3)$ versus $N_{simulated}(r,t_3)$ again with the 95% confidence interval. Panels a and b and d and e show that there is a general agreement in the spatial distribution and the relative values of the tumor cells in each voxel. Pearson's and concordance correlation coefficients for the voxels in the slice are 0.71 and 0.63, respectively. The Pearson and concordance correlation coefficients for all the voxels within the tumor for this patient are 0.70 and 0.65, respectively.

Pearson's correlation coefficient between the $N_{simulated}(r,t_3)$ and $N_{estimated}(r,t_3)$ for all the tumor voxels for each patient range from 0.38 to 0.70, and the concordance correlation coefficient range from 0.32 to 0.65. All Pearson's correlation coefficients were highly statistically significant ($P \ll 0.0001$). These results are summarized in Table 1.

For the ROI analysis, the mean number of cells at t_3 for both the simulated, $N_{simulated\_mean}(t_3)$, and the estimated, $N_{estimated\_mean}(t_3)$, number of cells with the 95% confidence interval are shown in Fig. 3. Pearson's correlation coefficient between $N_{simulated\_mean}(t_3)$ and $N_{estimated\_mean}(t_3)$ is 0.95 ($P = 0.004$) with a 95% confidence interval of 0.58 to 1.0. The range of the confidence interval is enlarged because the number of patients used is relatively small; however, Pearson's correlation is statistically significant and this indicates that there is a strong correlation between the simulated and the estimated number of cells on the last time point. The concordance correlation coefficient between $N_{simulated\_mean}(t_3)$ and $N_{estimated\_mean}(t_3)$ for all the patients is 0.83. This indicates that there is a strong agreement along the line of unity between $N_{simulated\_mean}(t_3)$ and $N_{estimated\_mean}(t_3)$.

Given the promising results in the ROI analysis, we hypothesized that the relatively weak correlation for the voxel level data may be due to SNR limitations and registration errors. Figure 4 shows cross sections through the tumors of the six patients at the three time points.

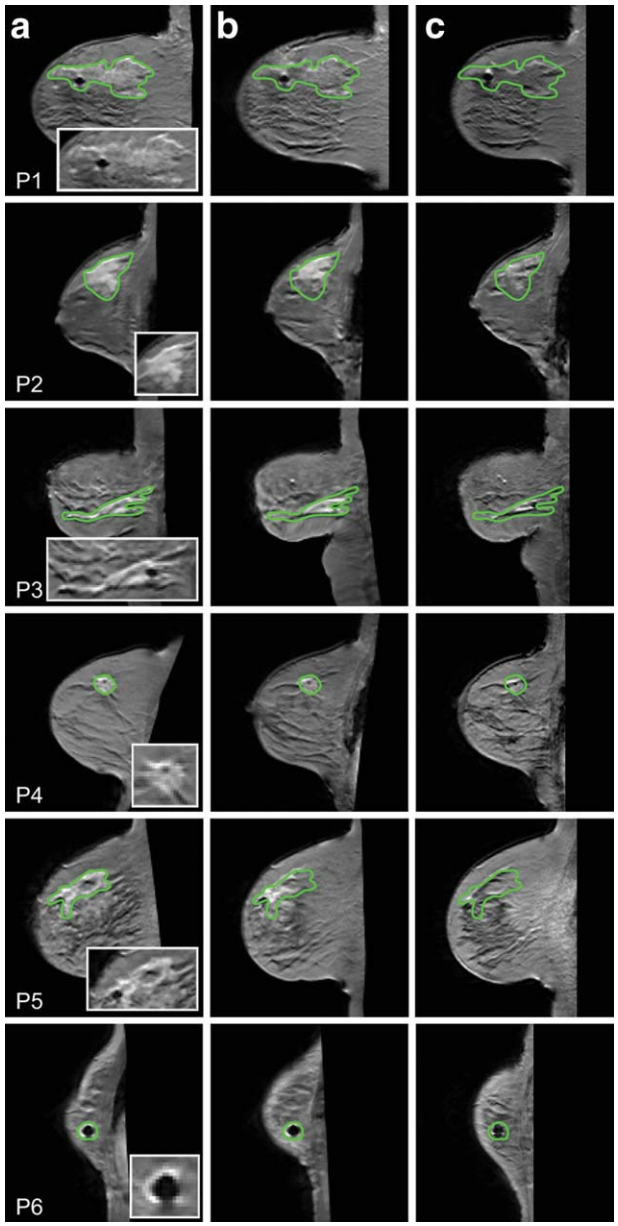

FIG. 4. Columns a (time point t_1), b (t_2), and c (t_3) display the registered postcontrast T_1-weighted images through the tumor for each patient for each imaging time point. A magnification of the tumor at t_1 is also shown in the first column. There is some misalignment in the tumor at the three time points for the patients and this may contribute to the relatively low correlations in the voxel level analysis found in some of the patients (see Table 1).

Columns a, b, and c show a single representative slice through the tumor of each patient at t_1, t_2, and t_3, respectively. There are slight misalignments in the tumors at the three time points and this may contribute to the relatively low-voxel level correlations found in some of the patients.

By smoothing the data, we reduce the effect of the registration errors and also increase the SNR, and an example is shown in Fig. 5. Column a is the estimated number of cells at t_3, column b is the simulated number of cells at t_3, and column c is a scatter plot of these data with the 95% confidence interval. Each row increases the kernel size and therefore the degree of smoothing. Pearson's and concordance correlation coefficients between the estimated and the simulated number of cells increase as the kernel size increases and this is summarized in Table 1. Pearson's correlation ranged from 0.38 to 0.70 for no filtering, and then 0.55 to 0.85, 0.69 to 0.96, and 0.76 to 0.98 for kernel sizes of 3×3, 6×6, and 9×9, respectively. The concordance correlation ranged from 0.32 to 0.65 for no filtering, and then 0.46 to 0.85, 0.55 to 0.95, and 0.60 to 0.98 for kernel sizes of 3×3, 6×6, and 9×9, respectively. All Pearson's correlation coefficients were highly statistically significant ($P \ll 0.0001$). As the kernel size increases, Pearson's correlation increases from weak to strong. This indicates that an increase in the SNR in the acquired DW-MRI data and/or improved accuracy in image registration may lead to an increase in both Pearson's and the concordance correlation coefficients between the estimated and the simulated number of cells at the last time point.

The salient features of the pathology reports for the patients are summarized in Table 2. The patients who had a complete response to the therapy appear to have a higher correlation between the simulated and the estimated number of cells at t_3 than patients with a partial response to the therapy, though the small patient number precludes a definitive conclusion.

DISCUSSION

We have shown how ADC values computed from DW-MRI data from breast cancer patients undergoing neoadjuvant chemotherapy can be used to estimate tumor cell proliferation values via the logistic model of tumor growth. The estimated proliferation rates were then used to predict tumor cellularity at the conclusion of therapy on both the voxel and ROI levels. The correlations between the simulated and the estimated number of cells on the last time point for the voxel-based analysis performed on individual patients showed weak to a moderately strong correlation. However, using the mean value of the ADC in the tumor ROI for the modeling resulted in a strong and significant relationship between the simulated and estimated data. We hypothesized that the strong relationship at the ROI level may be due to the inherent difficulties with acquiring high SNR DW-MRI data of the breast, as well as performing longitudinal registration of a deformable tissue such as the breast. To test this hypothesis, we smoothed the ADC values with a mean filter that resulted in a substantial increase in the strength of the correlation between simulated and estimated data as the size of the mean filter increases. This increase in the correlation, however, comes at the expense of losing some characterization of the spatial heterogeneity of ADC values within the tumors. Analysis with the mean ADC and the filtered ADC shows a much greater correlation between the estimated and simulated number of cells at the last time point. This shows the possibility of using sequential ADC data as a way to model tumor growth and treatment response if sufficient SNR and minimal registration error can be achieved.

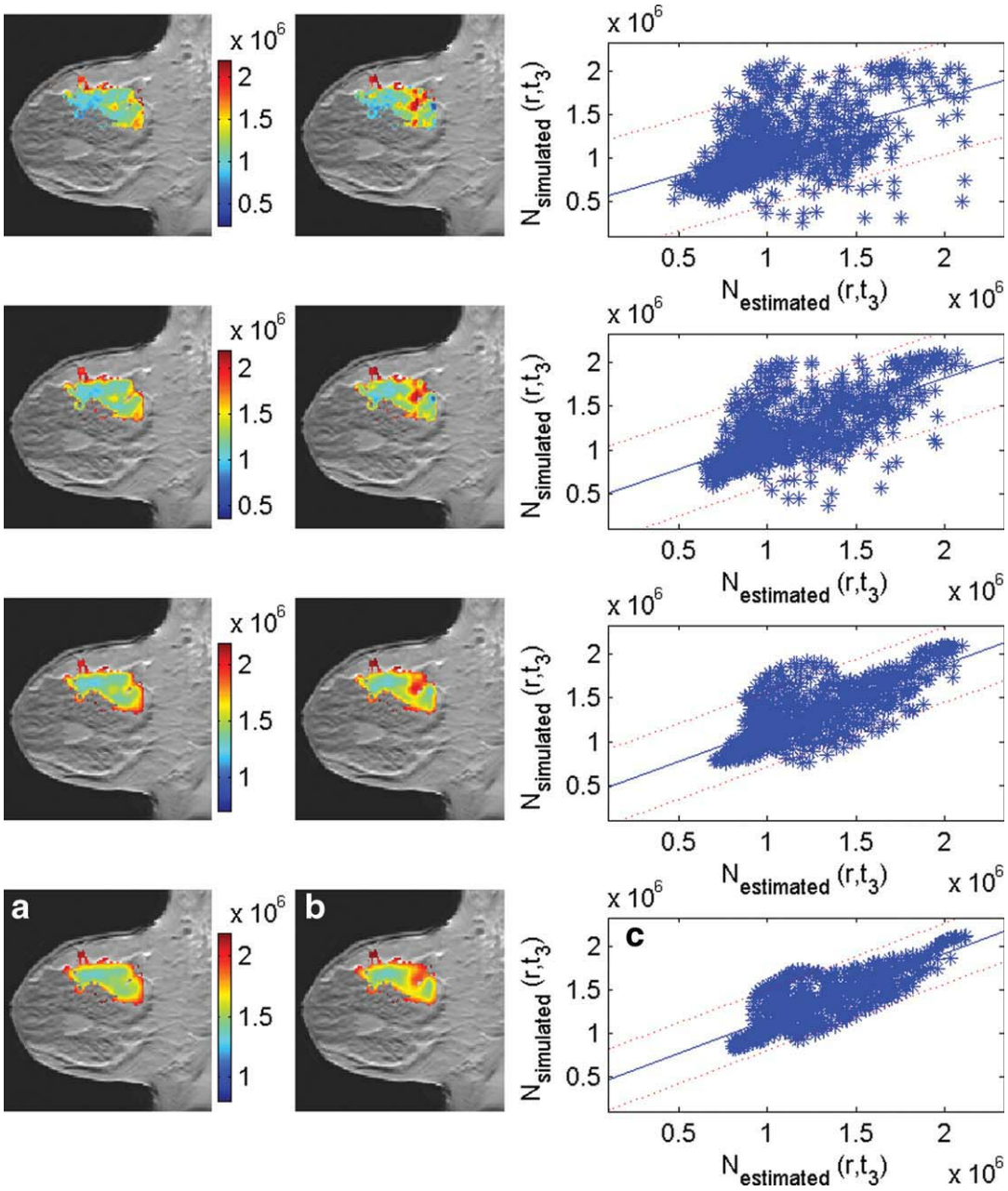

FIG. 5. Columns a and b display an overlay of the estimated and simulated number of cell at t_3, respectively, on a sagittal, T_1-weighted image slice through the tumor of a single patient. Column c displays the corresponding plots of the estimated and the simulated number of cells at t_3 with the 95% confidence interval displayed (red dashed lines). The rows (from top to bottom) correspond to different degrees of smoothing. Row 1 corresponds to the original image with no smoothing (Pearson's correlation $r = 0.51$ and $P \ll 0.0001$ between the estimated and the simulated number of cell at t_3 for the slice shown); row 2 corresponds to a convolution with a 3×3 averaging filter ($r = 0.65$ and $P \ll 0.0001$); row 3 corresponds to a convolution with a 6×6 averaging filter ($r = 0.75$ and $P \ll 0.0001$); and the last row corresponds to a convolution with a 9×9 averaging filter ($r = 0.81$ and $P \ll 0.0001$).

Table 2
Summary of the Key Histology Findings for Each Patient in the Study

Patients	Response	Histology grade	Proliferative rate	Estrogen	Progesterone	Her2
P1	Complete	High	High	−	−	+
P2	Incomplete	Intermediate	Intermediate	−	−	−
P3	Incomplete	High	Intermediate	−	−	−
P4	Incomplete	Intermediate	Low	−	−	−
P5	Complete	Low	Low	+	+	−
P6	Incomplete	High	Intermediate	−	−	−

Some of the limitations in the work include the small number of patients in the study and a number of simplifying assumptions. For example, we assumed that the proliferation rate can be predicted from the first two time points and that this rate remains constant over the course of treatment. Also, proliferation was modeled only on discrete days (days of treatment) in the cycle. We assumed that the change in ADC from the pretreatment image to the first post-treatment image was entirely due to the reduction in cellularity. We assumed that the voxels are comprised only tumor cells and as such we ignored the fact that each voxel most likely contains healthy breast and other supportive cells, as well as vascular spaces. We further assumed that the tumor cells can completely occupy a voxel, thereby ignoring the maximum packing fraction of the voxel that may undermine future efforts to correlate the modeling results with histology. Furthermore, we did not consider the size changes of the tumor during the course of therapy.

There are differences in the absolute values of the simulated and the estimated number of cells at the conclusion of therapy. Some of these differences may be due to slight misregistration between the tumors at the different time points, changes in the tumor proliferation rate during therapy, and the possible growth of healthy cells. Also, there may be distortions in the DW-MRI that are not present in the DCE-MRI and this may impact the accuracy of the tumor ROI transfer from DCE-MRI to DW-MRI.

Future improvements to the model will involve the incorporation of more biologically relevant tumor characteristics including the tissue volume fractions available from the DCE-MRI data, improvement in the registration between the tumors, and the comparison of the tumor cell count to histology.

CONCLUSION

Sequential ADC data can be used to predict tumor cell values at later time points. Improvement in the image quality and the image coregistration will lead to a better agreement between the estimated and the predicted tumor cells numbers at a later time point. To the best of our knowledge, this represents the first attempt to use imaging data to parameterize a mathematical model to predict changes in the cellularity of breast tumors during neoadjuvant chemotherapy.

ACKNOWLEDGMENTS

The authors thank Ingrid Mayer, M.D., Mark Kelley, M.D., Ingrid Meszoely, M.D., and Vandana Abramson, M.D. for many informative discussions.

REFERENCES

1. Fisher B, Bryant J, Wolmark N, Mamounas E, Brown A, Fisher ER, Wickerham DL, Begovic M, DeCillis A, Robidoux A, Margolese RG, Cruz AB Jr, Hoehn JL, Lees AW, Dimitrov NV, Bear HD. Effect of preoperative chemotherapy on the outcome of women with operable breast cancer. J Clin Oncol 1998;16 (8):2672–2685.
2. Sugahara T, Korogi Y, Kochi M, Ikushima I, Shigematu Y, Hirai T, Okuda T, Liang L, Ge Y, Komohara Y, Ushio Y, Takahashi M. Usefulness of diffusion-weighted MRI with echo-planar technique in the evaluation of cellularity in gliomas. J Magn Reson Imaging 1999;9 (1):53–60.
3. Chenevert TL, Stegman LD, Taylor JM, Robertson PL, Greenberg HS, Rehemtulla A, Ross BD. Diffusion magnetic resonance imaging: an early surrogate marker of therapeutic efficacy in brain tumors. J Natl Cancer Inst 2000;92 (24):2029–2036.
4. Hayashida Y, Hirai T, Morishita S, Kitajima M, Murakami R, Korogi Y, Makino K, Nakamura H, Ikushima I, Yamura M, Kochi M, Kuratsu JI, Yamashita Y. Diffusion-weighted imaging of metastatic brain tumors: comparison with histologic type and tumor cellularity. Am J Neuroradiol 2006;27 (7):1419–1425.
5. Anderson AW, Xie J, Pizzonia J, Bronen RA, Spencer DD, Gore JC. Effects of cell volume fraction changes on apparent diffusion in human cells. Magn Reson Imaging 2000;18 (6):689–695.
6. Lyng H, Haraldseth O, Rofstad EK. Measurement of cell density and necrotic fraction in human melanoma xenografts by diffusion weighted magnetic resonance imaging. Magn Reson Med 2000;43 (6):828–836.
7. Pickles MD, Gibbs P, Lowry M, Turnbull LW. Diffusion changes precede size reduction in neoadjuvant treatment of breast cancer. Magn Reson Imaging 2006;24 (7):843–847.
8. Sharma U, Danishad KKA, Seenu V, Jagannathan NR. Longitudinal study of the assessment by MRI and diffusion-weighted imaging of tumor response in patients with locally advanced breast cancer undergoing neoadjuvant chemotherapy. NMR Biomed 2009;22 (1):104–113.
9. Yankeelov TE, Lepage M, Chakravarthy A, Broome EE, Niermann KJ, Kelley MC, Meszoely I, Mayer IA, Herman CR, McManus K, Price RR, Gore JC. Integration of quantitative DCE-MRI and ADC mapping to monitor treatment response in human breast cancer: initial results. Magn Reson Imaging 2007;25 (1):1–13.
10. Ellingson BM, LaViolette PS, Rand SD, Malkin MG, Connelly JM, Mueller WM, Prost RW, Schmainda KM. Spatially quantifying microscopic tumor invasion and proliferation using a voxel-wise solution to a glioma growth model and serial diffusion MRI. Magn Reson Med 2011;65 (4):1131–1143.
11. Konukoglu E, Clatz O, Menze BH, Stieltjes B, Weber MA, Mandonnet E, Delingette H, Ayache N. Image guided personalization of reaction-diffusion type tumor growth models using modified anisotropic eikonal equations. IEEE Trans Med Imaging 2010;29 (1):77–95.
12. Hogea C, Davatzikos C, Biros G. Modeling glioma growth and mass effect in 3D MR images of the brain. Medical image computing and computer-assisted intervention—MICCAI 2007. Vol. 4791. Springer: Berlin/Heidelberg; 2007. pp 642–650.
13. Hogea C, Davatzikos C, Biros G. An image-driven parameter estimation problem for a reaction–diffusion glioma growth model with mass effects. J Math Biol 2008;56 (6):793–825.
14. Jbabdi S, Mandonnet E, Duffau H, Capelle L, Swanson KR, Pelegrini-Issac M, Guillevin R, Benali H. Simulation of anisotropic growth of low-grade gliomas using diffusion tensor imaging. Magn Reson Med 2005;54 (3):616–624.
15. Atuegwu NC, Gore JC, Yankeelov TE. The integration of quantitative multi-modality imaging data into mathematical models of tumors. Phys Med Biol 2010;55 (9):2429–2449.
16. Yankeelov TE, Atuegwu NC, Deane NG, Gore JC. Modeling tumor growth and treatment response based on quantitative imaging data. Integr Biol 2010;2:338–345.
17. Stejskal EO, Tanner JE. Spin diffusion measurements: spin echoes in the presence of a time-dependent field gradient. J Chem Phys 1965; 42 (1):288–292.
18. Li X, Dawant BM, Welch EB, Chakravarthy AB, Xu L, Mayer I, Kelley M, Meszoely I, Means-Powell J, Gore JC, Yankeelov TE. Validation of an algorithm for the nonrigid registration of longitudinal breast MR images using realistic phantoms. Med Phys 2010;37 (6):2541–2552.
19. Li X, Dawant BM, Welch EB, Chakravarthy AB, Freehardt D, Mayer I, Kelley M, Meszoely I, Gore JC, Yankeelov TE. A nonrigid registration algorithm for longitudinal breast MR images and the analysis of breast tumor response. Magn Reson Imaging 2009;27 (9):1258–1270.
20. Byrne HM. Modelling avascular tumor growth. In: Preziosi L, editor. Cancer modelling and simulation. Boca Raton, FL: Chapman and Hall/CRC Mathematical Biology and Medicine Series; 2003. pp 75–120.
21. Lin LI. A concordance correlation coefficient to evaluate reproducibility. Biometrics 1989;45 (1):255–268.